Geofísica Internacional (2024) **63-2**: 817 - 834

Forward modeling of spectral gamma-ray (SGR) logging in sedimentary formations

Lechuga-Lagos F.M.[1], Aquino-López A.[*2], Valdez-Grijalva M.A.[2] and Campos-Enriquez J.O.[3]

Abstract

We propose a new approach to improve spectral gamma-ray (SGR) logging forward modeling by considering the radioactive minerals present in the rock as gamma-ray sources. This is based on the radioactive attenuation theory. The assumptions are: 1) minerals with K^{40}, U^{238}, and Th^{232} content are considered radioactive sources uniformly distributed in the rock; 2) the measured radioactivity is proportional to the concentration of radioactive minerals and inversely proportional to the rock bulk density; 3) the radioactivity is only attenuated by absorption of gamma-rays. The forward modeling was tested using a synthetic case of sandstone with clay minerals and brine-saturated pores to analyze the sensitivity of SGR to changes in illite/smectite-illite/mica ratios and sandstone porosities. Finally, it was further validated with 44 core samples, of which 22 are from two shale gas and 22 from two clastic formations. The Pearson correlation coefficient applied to measure the misfit between the simulated and observed K, U, Th, and SGR data attained values of 0.82, 0.83, 0.61, and 0.57, respectively. A further improvement to 0.87, 0.85, 0.65, and 0.69 was achieved when applying joint inversion for data where illite/smectite and illite/mica ratios were not specified. The correlation between the simulated and observed data supports the viability of the proposed SGR forward modeling approach method.

Key words: Spectral gamma-ray logging, Forward modeling, Radioactive minerals, Sedimentary formations, K^{40}, U^{238}, Th^{232} radioisotopes.

Resumen

Proponemos un nuevo enfoque para mejorar el modelado directo del registro de rayos gamma espectral (SGR) al considerar los minerales radioactivos presentes en la roca como fuentes de rayos gamma. Este se basa en la teoría de la atenuación radiactiva. Los supuestos son: 1) los minerales con contenido de K^{40}, U^{238}, y Th^{232} son considerados fuentes radiactivas que están uniformemente distribuidas en la roca; 2) la radiactividad medida es proporcional a la concentración de minerales radiactivos e inversamente proporcional a la densidad aparente de la roca; 3) la radiactividad solo se atenúa por absorción de rayos gamma. El modelado directo fue probado usando un caso sintético de arenisca con minerales arcillosos y poros saturados con salmuera para analizar la sensibilidad de SGR a cambios en las relaciones de ilita/esmectita e ilita/mica y porosidades de la arenisca. Finalmente, el enfoque fue validado con 44 muestras de núcleo, siendo 22 de dos formaciones de gas en lutita y 22 de dos formaciones clásticas. El coeficiente de correlación de Pearson se aplicó para medir el desajuste entre los datos simulados y medidos de K, U, Th y SGR, obteniéndose valores de 0.82, 0.83, 0.61 y 0.57 respectivamente, y una mejora adicional de 0.87, 0.85, 0.65 y 0.69, respectivamente. Estos resultados fueron alcanzados aplicando inversión conjunta para los datos donde las relaciones ilita/esmectita e ilita/mica no fueron especificadas. La correlación lograda entre los datos simulados y observados sustenta la viabilidad del nuevo enfoque para el modelado directo propuesto de SGR.

Palabras clave: Registro de rayos gamma espectral, Modelado directo, Minerales radioactivos, Formaciones sedimentarias, Radioisótopos K^{40}, U^{238}, Th^{232}.

Received: May 16, 2023 ; Accepted: November 15, 2023; Published on-line: April 1, 2024.

Editorial responsibility: Dr. Oscar C. Valdiviezo-Mijangos

* Corresponding author: Ambrosio Aquino López. E-mail: aaquino@imp.mx
[1] Posgrado del Instituto Mexicano del Petróleo, Instituto Mexicano del Petróleo, Ciudad de México (CDMX), México.
[2] Geofísica Cuantitativa, Instituto Mexicano del Petróleo, Ciudad de México (CDMX), México.
[3] Instituto de Geofísica, Universidad Nacional Autónoma de México, Ciudad de México (CDMX), México.

Francisco Miguel Lechuga Lagos, Ambrosio Aquino López, Miguel Ángel Valdez Grijalva, José Oscar Campos Enríquez.

https://doi.org/10.22201/igeof.2954436xe.2024.63.1.1710

1. Introduction

Sedimentary rocks contain radioisotopes that emit radiation due to nuclear decay. In geophysical logging applications, the gamma-ray spectrum is of primary interest due to its high penetration into rock, which is approximately inversely proportional to the atomic number of the elements which make up the rock through which it travels, which allows gamma rays to be recorded by an instrument (Bassiouni, 1994; Schön, 2015; Serra, 1984; Owen, 1966). The radioisotopes which are significant in sedimentary rocks are K^{40} (half-life time of 4.4×10^{9} years), Th^{232} (half-life time of 1.4×10^{10} years), and U^{238} (half-life time of 1.3×10^{9} years). These decay into Ar^{40}, Pb^{208}, and Pb^{206}, emitting radiation with energies of 1.46 MeV, 2.62 MeV, and 1.76 MeV, respectively (Bassiouni, 1994; Schön, 2015; Serra, 1984).

Estimating radioactive elements is critical in rock formation evaluation since it assists lithology identification of many clay minerals (Bassiouni, 1994; Schnyder *et al.*, 2006; Ellis and Singer, 2007; Schön, 2015). SGR logging allows a quantitative evaluation of K, U, and Th concentrations by decomposing the total radioactive spectra into the three characteristic spectra (Brannon and Osoba, 1956; Lock and Hoyer, 1971; Serra *et al.*, 1980; Serra, 1984; Mathis *et al.*, 1984; Bassiouni, 1994).

The total gamma-ray contribution is obtained by the sum of the radioactivity of K, U, and Th (Bassiouni, 1994; Schön, 2015; Serra *et al.*, 1980). Assessment of the presence of these radioisotopes is helpful in the determination of lithology because they are usually concentrated in carbonate minerals, clay minerals, organic matter, potassium feldspars, and evaporites, as well as in heavy minerals (Schön, 2015; Ellis and Singer, 2007; Bassiouni, 1994; Serra *et al.*, 1980; Fertl, 1979; Russell, 1945).

SGR logging is applied in conventional formations (sandstone and carbonate rocks) to differentiate between reservoir and non-reservoir rocks, to recognize the evaporite mineral, to identify rock mineral types, and help evaluation of their concentration by either cross-plot or computation (Fertl *et al.*, 1982; Bassiouni, 1994; Schön, 2015; Serra, 1984). It also allows the identification of zones containing organic material in unconventional reservoirs (Huang *et al.*, 2015; Lüning and Kolonic, 2003; Swanson, 1960; Bohacs, 1998; Bohacs and Miskell-Gerhardt, 1998; Ge *et al.*, 2016; Jacobi *et al.*, 2008), and the identification of fractured reservoirs (Fertl, 1979; Fertl and Rieke III, 1980). Further, the Th/K or Th/U ratios are used as qualitative indicators of the principal radioactive mineral contained in the rock (Bassiouni, 1994; Serra *et al.*, 1980; Schön, 2015) and to identify sedimentary facies (Adams and Weaver, 1958; Bigelow, 2002).

Empirical equations to estimate shale content by assuming that only clay minerals emit gamma radiation (Larionov, 1969; Stieber, 1970; Clavier *et al.*, 1971) and to estimate organic material content in unconventional reservoirs considering mainly the U concentration (Wang *et al.*, 2019, 2016; Steiner *et al.*, 2016; Gonzalez *et al.*, 2013; Schmoker, 1981) were derived by different authors. However, sedimentary formations contain different radioactive minerals (Bigelow, 2002). Sandstones and carbonates can contain other radioactive minerals besides clay (Chudi and Simon, 2012; Schön, 2015). Shale gas formations exhibit a high content of K, U, and Th due to the presence of clay and plagioclase minerals (Huang *et al.*, 2015; Lüning and Kolonic, 2003; Passey *et al.*, 1990, 2010; Russell, 1945; Alharthy *et al.*, 2012). Therefore, the concentration of organic matter could be overestimated by not separating the U present in the clay and plagioclase (Lüning and Kolonic, 2003; Schnyder *et al.*, 2006). Th/K and Th/U ratios do not help as a facies discriminator if they are approximately constant in the studied lithofacies (North and Boering, 1999). Estimation of the concentration of radioactive minerals can be approximated by linearly correlating SGR signals with compressional travel time (Δt), bulk density (ρ_b), or neutron porosity (ϕ_N) logs, and it is strengthened with information from lithological and geochemical logging, Scanning Electron Microscope images (SEM), and X-ray diffraction in cores (Day-Stirrat *et al.*, 2021; Chudi and Simon, 2012; Hertzog *et al.*, 1989). The inadequate quantification of the concentration of radioactive minerals leads to increased uncertainty in the estimation of reservoirs (GaffneyCline, 2023).

We are interested in quantifying radioactive minerals from SGR signals without using empirical equations. In this context, forward modeling of natural gamma rays has been done considering multiple radioactive minerals (Serra, 1984; Bassiouni, 1994; Ellis and Singer, 2007) but is limited to modeling the total radioactivity of a given formation. SGR simulation has been applied to derive source rock characteristics and examine diagenesis by reconstructing part of the sedimentary rock history without focusing on quantifying radioactive minerals (Van der Boor, 2014).

In this work, we present an approach to SGR logging forward modeling that considers radioactive minerals present in the rock as gamma-ray sources, and it is based on radioactivity attenuation theory. The forward modeling is based on the following assumptions: 1) minerals with K^{40}, Th^{232}, and U^{238} content are considered radioactive sources uniformly distributed in the rock; 2) the measured radioactivity is proportional to the concentration of radioactive minerals and inversely proportional to the rock bulk density; 3) the radioactivity is only attenuated by absorption of gamma-rays.

Some minerals are bound together, such as illite/smectite and illite/mica, so their concentration is reported jointly in the petrographic analysis of cores without specifying the specific content of each mineral. For this reason, the SGR modeling approach is tested through a synthetic control rock of sandstone with clay minerals of illite/smectite and illite/mica mixtures and brine-saturated pores to analyze the sensitivity of SGR to changes in illite/smectite-illite/mica ratios and sandstone porosities.

We further tested the SGR forward modeling on 44 core samples, 22 corresponding to two shale gas and 22 to two clastic formations, to validate it. Pearson correlation coefficient was applied to analyze the misfit between the simulated and observed U, K, Th, and SGR data, attaining values of 0.82, 0.83, 0.61, and 0.57, respectively. Joint inversion was applied in those cases where corresponding ratios of illite/smectite and illite/mica were unavailable, leading to an improvement of Pearson correlation coefficient of 0.87, 0.85, 0.65 and 0.69, respectively, for U, K, Th, and SGR.

2. Theoretical background

In this section, we describe the basics of SGR logging to quantify the presence of K, Th, and U; and the physical basis of the proposed modeling considering minerals as radioactive sources.

2.1 SGR logging basics

The K^{40}, Th^{232}, and U^{238} radioisotopes are abundant in sedimentary rocks and have respective half-lives of 4.4×10^9, 1.4×10^{10}, and 1.3×10^9 years, respectively, so their presence in the rock is sufficiently long-lived, and they produce appreciable amounts of gamma rays (Bassiouni, 1994; Hertzog *et al.*, 1989; Bigelow, 2002; Serra, 1984; Schön, 2015). These radioisotopes are contained in different proportions in the radioactive minerals of petroleum reservoirs (Lock and Hoyer, 1971; Killeen, 1982; Serra, 1984; Bassiouni, 1994; Schön, 2015). K^{40}, Th^{232}, and U^{238} radioisotopes have characteristic energies emitted in discrete values of 1.46 MeV, 2.62 MeV, and 1.76 MeV, respectively, and they are contained in specific minerals that are assumed to be uniformly distributed in the sedimentary formation (Rhodes and Mott, 1966; Bassiouni, 1994; Serra, 1984; Schön, 2015).

Gamma-ray logging aims to measure the total number of gamma rays emitted by the rock formation per second per unitary weight (Belknap *et al.*, 1959). Its general configuration consists of a gamma ray detector, a processor, a memory, a telemetry module, and a surface acquisition system (Morys, 2020; Morys, 2021). The signal from the detector is amplified and discretized in energy levels or windows which span a specific energy band. The data is then encoded and sent to a surface acquisition system (Brannon and Osoba, 1956; Lock and Hoyer, 1971; Serra *et al.*, 1980; Serra, 1984; Mathis *et al.*, 1984; Bassiouni, 1994).

Three energy windows are associated with the characteristic energies of K^{40}, Th^{232}, and U^{238}, and their fractional abundances are computed by:

$$\sum_{i=1}^{n} r_i^2 = \sum_{i=1}^{n}\left(W_i - A_i Th^{232} - B_i \mathrm{U}^{238} - C_i \mathrm{K}^{40}\right)^2 = r^2 \quad (1)$$

where r_i is a factor representing a statistical error, W_i is the count-rate from window *i*, and A_i, B_i and C_i are the calibrated coefficients for the respective window i obtained by using a calibration "TUK" pit by minimizing Equation 1 (Serra, 1984, p. 120).

2.2 Physical basis of gamma radiation for radioactive minerals

This section describes the modeling of gamma-ray activity from K^{40}, U^{238}, and Th^{232}, considering them hosted in certain minerals, and that the medium (in this case, the rock) attenuates the gamma-ray flux.

In gamma radiation, a photon is emitted after a nucleus decays. The law of radioactive decay states that over a short time interval, dt, the number of decaying radioisotopes obeys the following expression (Rutherford and Soddy, 1902):

$$\frac{dN}{dt} = -\lambda N\ , \quad (2)$$

where N is the number of atoms of the radioisotope and λ (s^{-1}) is the decay constant. Integrating Equation 2 leads to the exponential relation:

$$N = N_0 e^{-\lambda t}, \quad (3)$$

where N_0 is the number of radioisotopes present at time $t = 0$. The activity A, the rate at which nuclei are decaying, is obtained by:

$$A=\lambda N \quad (4)$$

The specific activity (a) is a more widely used parameter which is defined as the net gamma counts per second measured from a gram of a radioisotope in equilibrium (s^{-1}). For the K^{40}, U^{238}, and Th^{232} series, it is obtained by summing the measured contributions from each of the radioisotopes considering only photons with energy greater than 100 keV (Belknap *et al.*, 1959; Ehsan *et al.*, 2019; Bassiouni, 1994). Their respective specific activities are: a_K=3.4 s^{-1}, a_U=2.8×10^4 s^{-1}, and a_{Th}=1.0×10^4 s^{-1} (Belknap *et al.*, 1959).

In a sedimentary rock a can be considered as (Belknap *et al.*, 1959):

$$a=a_K K+a_U U+a_{Th} Th, \quad (5)$$

being K (%), U (ppm), and Th (ppm) the fractional abundances of K^{40}, U^{238}, and Th^{232} in the rock (Serra, 1984; Ellis and Singer, 2007; Schön, 2015).

The radioactive activity of *m* minerals in a volume dV, considering them as sources, as a function of the fractional abundance of *n* radioisotopes for a control volume is obtained by:

$$dS_{ij} = \left[\sum_{i}^{m} \sum_{j}^{n} C_j \rho_i w_j^i a_j \right] dV \tag{6}$$

$C_i \left(\sum_{i=1}^{n} C_i = 1 \right)$ and ρ_i are the fractional concentration in the control volume, and density of the *i*-th mineral, respectively. w_j^i is the fractional abundance of the *j*-th radioisotope in the *i*-th mineral and a_j is the specific activity of the *j*-th radioisotope. We consider that the radioactive minerals are uniformly distributed.

Considering the radioactive attenuation theory, the total emissions are obtained by (Ellis and Singer, 2007; Evans, 1955):

$$d\phi(r) = \left[\sum_{i}^{m} \sum_{j}^{n} C_j \rho_i w_j^i a_j \right] \frac{e^{-\mu_a r}}{4\pi r^2} dV \ , \tag{7}$$

being $e^{-\mu a\, r}$ the attenuation factor and μa (cm^{-1}) the macroscopic absorption cross section (Duderstadt and Hamilton, 1976; Rhodes and Mott, 1966; Evans, 1955). The entire spherical source is obtained integrating over the solid angle Ω, thus $\int_{\Omega} dA = 4\pi r^2$. The total gamma-ray flux that reaches to the detector is given by:

$$\phi = \left[\sum_{i}^{m} \sum_{j}^{n} C_i \rho_i w_j^i a_j \right] \int_0^{\infty} e^{-\mu_a r} dr = \left[\sum_{i}^{m} \sum_{j}^{n} C_i \rho_i w_j^i a_j \right] \frac{1}{\mu_a} , \tag{8}$$

and the count rate R through (Evans, 1955):

$$R = \epsilon \frac{\mu_a}{\rho_b} \phi \frac{\epsilon}{\rho_b} \left[\sum_{i}^{m} \sum_{j}^{n} C_i \rho_i w_j^i a_j \right], \tag{9}$$

where ϵ is the efficiency of the gamma-ray sensor, the probability that a gamma-ray incident to the detector will produce a count (Belknap *et al.*, 1959; Rhodes and Mott, 1966), and ρ_b is the rock bulk density.

To calculate the count rate in API units and considering only the radioisotopes of our interest: K^{40}, U^{238}, and Th^{232}, Equation 9 can be simplified in the following equation:

$$SGR = \frac{\epsilon}{\rho_b} \sum_{i}^{m} C_i \rho_i \left(K^i \eta + U^i \alpha + Th^i \beta \right), \tag{10}$$

where the coefficient η, β, and α depend on the detector and sonde design and normalized a_{Th} and a_K to a_U (the concentration of U in ppm that give the exact count rate as 1% of K and 1 ppm of Th). K_i, U_i, and Th_i are the fractional abundances of K^{40}, U^{238}, and Th^{232}, respectively, in the *i*-th mineral.

Further, Equation 10 can be rewritten in the standard form (Belknap *et al.*, 1959; Bassiouni, 1994; Ellis and Singer, 2007; Schön, 2015):

$$SGR = \epsilon(\eta K + \alpha U + \beta Th), \tag{11}$$

being K, U, and Th, the total content of K^{40}, U^{238}, and Th^{232} in the rock, respectively, and modeled as:

$$K = \frac{1}{\rho_b} \sum_{i}^{m} C_i \rho_i K^i \ , \tag{12}$$

$$U = \frac{1}{\rho_b} \sum_{i}^{m} C_i \rho_i U^i \ , \tag{13}$$

$$Th = \frac{1}{\rho_b} \sum_{i}^{m} C_i \rho_i Th^i \ . \tag{14}$$

3. SGR forward modeling

The petrophysical model underlying the proposed SGR forward modeling comprises pores, radioactive minerals, and nonradioactive minerals. The radioactive minerals have characteristic fractional abundances of K^{40}, U^{238}, and Th^{232} in specific ranges for each mineral, which were considered for forward modeling (Table 1).

The SGR forward modeling is done with Equation 10 and tested: 1) against a synthetic control rock of sandstone with clay minerals and brine-saturated pores to analyze the sensibility of the SGR to changes in illite/smectite, illite/mica ratios, and sandstone porosities; and 2) against 44 core samples of which 22 are from two shale gas formations and 22 from two clastic formations to validate it.

3.1 Synthetic case

We consider a sandstone with clay minerals and brine-saturated pores. The sandstone comprises 80% of solid grains

Table 1. Range of fractional abundances *K*, *U*, and *Th* in some radioactive minerals (Schön, 2015; Bigelow, 2002; Huntley and Baril, 1997; Yuguchi *et al.*, 2021; Sen, 1959; Lewis *et al.*, 2004). Void entries in the table indicate the absence of the respective radioisotope.

Mineral	***K*** **(%)**	***U*** **(ppm)**	***Th*** **(ppm)**	$\rho\left(\frac{g}{cm^3}\right)$
Quartz	< 0.15	< 0.4	< 2.0	2.648
Calcite	< 0.4	1.5 – 15	< 2.0	2.71
Dolomite	0.1 – 0.3	1.5 – 10	< 2.0	2.86
K-feldspar	11.8 – 14	0.2 – 5.0	0.01 – 7.0	2.56
Plagioclase	< 0.54	0.02 – 5.0	0.01 – 3.0	2.68
Mica (Biotite)	6.2 – 10.1	1 – 40	0.5 – 50	2.8
Illite	3.5 – 8.3	1 – 5	10 – 20	2.66
Smectite	0 – 1.5	1 – 21	6 – 44	2.2
Kaolinite	0 – 0.6	1 – 12	6 – 47	2.594
Chlorite	0 – 0.35	–	3 – 5	2.8
Kerogen	–	62.5 – 500	–	1.1 – 1.4

(quartz) and 20% of pores. To increase the clay concentration, we replaced equivalent concentrations of sandstone. Only clay minerals are radioactive.

We analyze the K, U, Th, and SGR forward modeling in two scenarios: a) a sandstone with a mixture of illite/smectite and b) a sandstone with an illite/mica mixture. Scenario a) comprised: 1) clay of 100% of illite, 2) clay of 100% of smectite, and 3) clay with a proportion of 50 to 50% of illite and smectite. Scenario b) comprised: 1) clay of 100% of illite, 2) clay of 100% of mica, and 3) clay with a proportion of 50 to 50% of illite and mica. All possible illite/smectite and illite/mica ratios are bounded by 1 and 2 in scenarios "a" and "b", respectively. The fractional abundances *K*, *U*, and *Th* and the density used for the respective radioactive minerals are shown in Table 2. The K, U, and Th content were modeled with Equations 12, 13, and 14, respectively, and SGR was modeled with Equation 10.

K content obtained from illite/smectite ratios is broader than those obtained with illite/mica ratios for each clay concentration (Figure 1). In addition, it can be observed that K values in illite/smectite mixtures are lower compared to illite/mica mixtures (Figure 1). This is evident from the reference lines depicting 50 to 50% of the illite/smectite mixture and 100% of smectite (Figure 1a), which show lower K values than the reference lines of 50 to 50% of the illite/mica mixture and 100% of mica (Figure 1b).

U content from illite/smectite and illite/mica ratios are in a similar range below 18% of clay concentration (less than 1%

Table 2. Fractional abundances *K*, *U*, and *Th* and density used for synthetic case forward modeling.

Mineral	***K*** **(%)**	***U*** **(ppm)**	***Th*** **(ppm)**	$\rho\left(\frac{g}{cm^3}\right)$
Illite	8.3	5	20	2.66
Smectite	1.5	21	44	2.2
Mica	6.2	16.9	27	2.8

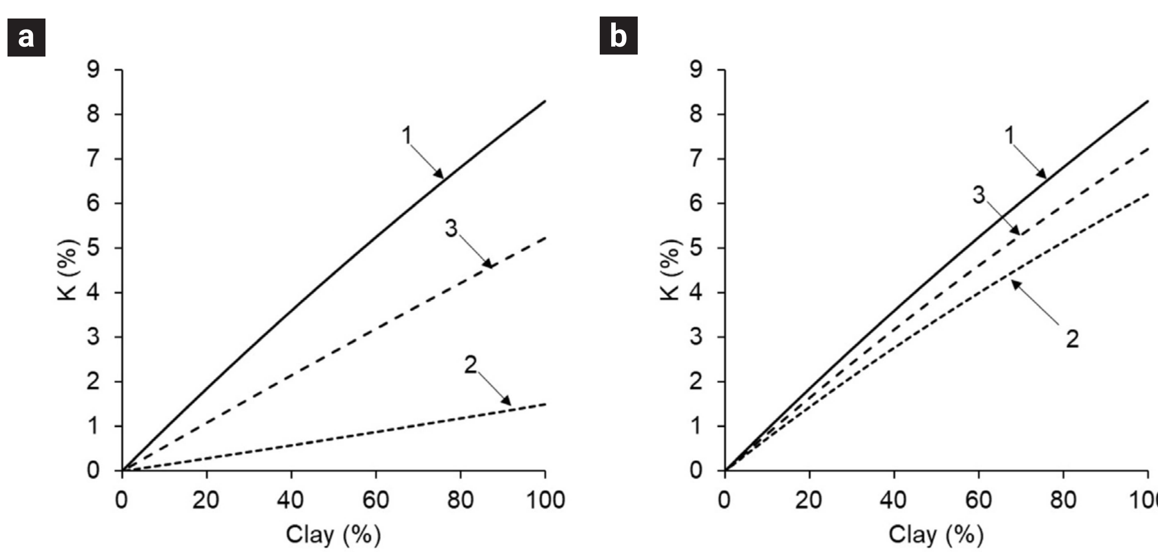

Figure 1. K content for mixtures of a) illite/smectite and b) illite/mica. a) K for clay constituted by illite (line 1), smectite (line 2), and 50 to 50% of illite/smectite (line 3). b) K for clay constituted by illite (line 1), mica (line 2), and 50 to 50% of illite/mica (line 3).

absolute difference), but above 18% are higher (Figure 2). The reference lines for 50 to 50% of the illite/smectite mixture and 100% of smectite compared to 50 to 50% of illite/mica and 100% of mica, respectively, show that the U values for scenario "a" (Figure 2a) are slightly higher than scenario "b" (Figure 2b).

Th content from illite/smectite ratios has a broader range than illite/mica ratios for each clay concentration (Figure 3). The reference lines for 50 to 50% of illite/smectite mixture and 100% of smectite (Figure 3a) give higher Th values than 50 to 50% of illite/mica mixture and 100% of mica (Figure 3b), indicating that Th values for scenario "a" are higher than scenario "b".

SGR for scenario "a" has a similar range to scenario "b" (Figure 4). The reference lines for 50 to 50% of illite/smectite mixture and 100% of smectite (Figure 4a) are slightly higher for SGR values than 50 to 50% of illite/mica mixture and 100% of mica (Figure 4b). Furthermore, the relationships between SGR and clay concentration are not linear for both scenarios due to the differences in their bulk densities.

We further analyzed the effect of porosity changes on the SGR considering sandstone porosities of 1) 45%, 2) 25%, and 3) 5% and clay with a 50 to 50 % proportion of illite/mica (Figure 5) since changes in porosities impact directly over ρ_b, which in turn affects the radioactive response. The SGR radioactive intensity is lower as the ρ_b is higher (Schmoker, 1979).

These results show that considering K, U, Th, and SGR for the presented synthetic case improve the contrast to identify mineral mixtures that only regard SGR (in this case, illite/smectite and illite/mica), and this analysis can be generalized to other mixtures of associated minerals. Further, the nonlinear trend between SGR versus clay concentration depends on the rock's bulk density.

3.2 SGR forward modeling applied to core samples

3.2.1 Sample descriptions

We applied the SGR forward modeling to 44 core samples, of which 14 are from Well A and 8 from Well G (Sabinas and Burgos provinces, respectively, in Mexico), both corresponding to shale gas formations and 19 were taken from Well N (Cordilleras Mexicanas province) and 3 from Well Q (North Sea, Netherlands), both corresponding to clastic formations. The data considered for modeling are the concentrations of porosity, quartz, calcite, dolomite, pyrite, feldspars: K-feldspar and plagioclase, total clay: proportions of illite/smectite and illite/mica, kaolinite, chlorite, and kerogen (Table 3). The porosity was obtained from the petrophysical analysis, the mineralogical concentration was provided by thin section petrography and X-ray diffraction (XRD), and the kerogen concentration was calculated through the Total Organic Carbon (TOC) reported in geochemical data, considering that the kerogen concentration is approximately twice that of the TOC (Kethireddy *et al.*, 2014; Passey *et al.*, 2010; Schmoker, 1981). We consider kerogen for the gamma-ray forward modeling even though it is not a mineral because it has a high uranium concentration (Lüning and Kolonic, 2003). The ρ_b, SGR and K, U, and Th fractional abundances for each core sample were obtained from Well logs (Table 4).

The core samples from Well A correspond to a calcareous silty shale. The porosity measured is between 2.03 to 12.26%, saturated mainly by gas. The minerals present in the rock are quartz, calcite, dolomite, pyrite, K-feldspar, plagioclase, proportions of illite/smectite and illite/mica, kaolinite, and kerogen as an organic component which is the ranges of 0.58-12.22%. The

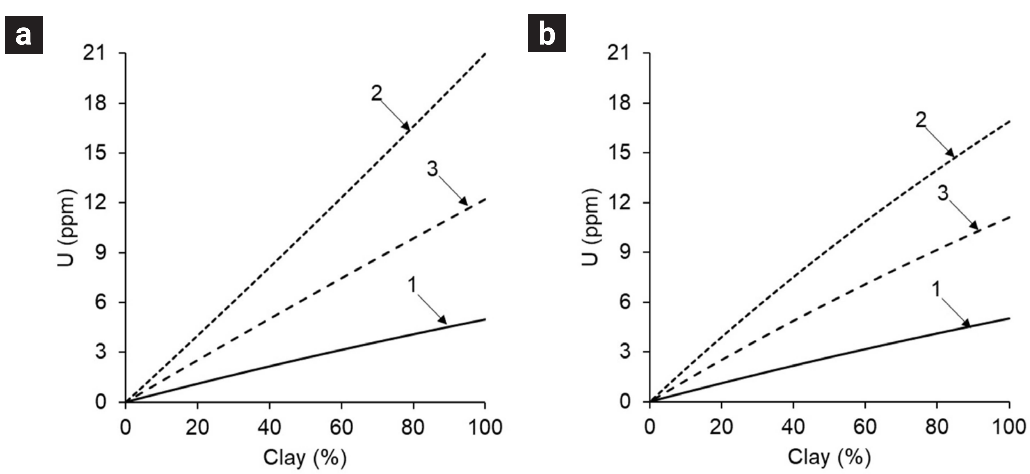

Figure 2. U content for mixtures of a) illite/smectite and b) illite/mica. a) U for the clay of illite (line 1), smectite (line 2), and 50 to 50% of illite/smectite (line 3). b) U for the clay of illite (line 1), mica (line 2), and 50 to 50% of illite/mica (line 3).

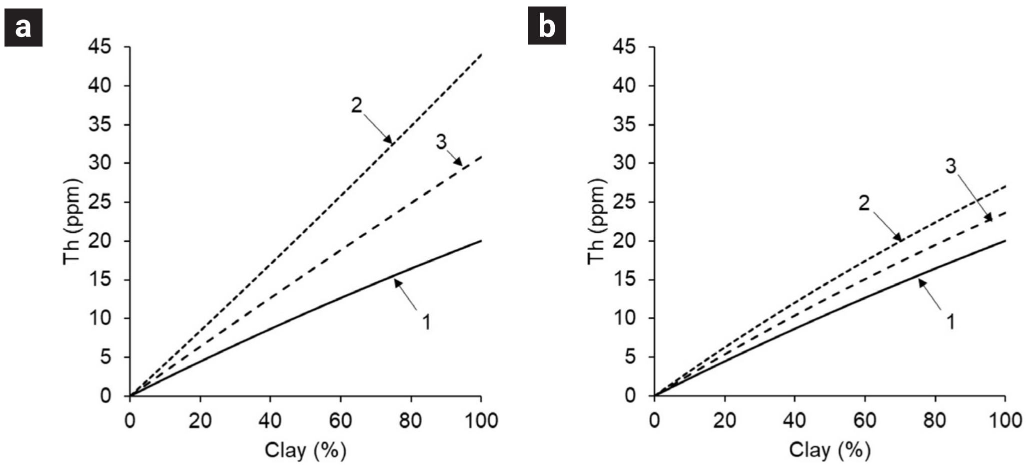

Figure 3. The content for mixtures of a) illite/smectite and b) illite/mica. a) Th for clay constituted illite (line 1), smectite (line 2), and 50 to 50% illite/smectite. b) Th for clay constituted by: illite (line 1), mica (line 2), and 50 to 50% of illite/mica (line 3).

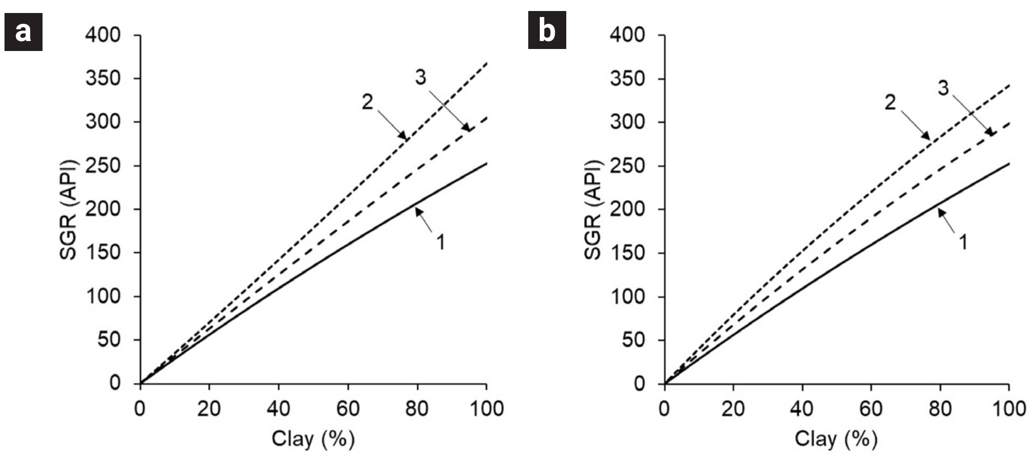

Figure 4. SGR modeled for mixtures of a) illite/smectite and b) illite/mica. a) SGR for a clay constituted by: illite (line 1), smectite (line 2), and 50 to 50% of illite/smectite (line 3). b) SGR for a clay constituted of illite (line 1), mica (line 2), and 50 to 50% of illite/mica (line 3).

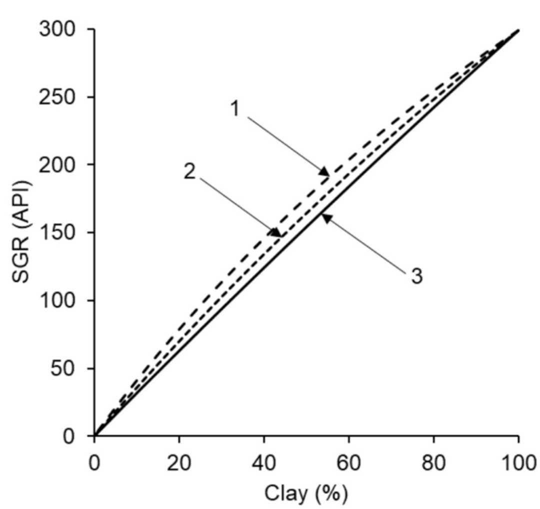

Figure 5. SGR modeled for a 50 to 50% proportion of illite/mica. Line 1: Sandstone with a density of 1.91 g/cm^3, 55% of quartz grains and 45% of pores; line 2: density range of 2.24 g/cm^3, 75% of quartz grains and 25% of pores; and line 3: a density of 2.56 g/cm^3, 95% of quartz grains and 5% of pores.

Table 3. Data from 44 core samples. Concentration in %. Void entries indicate the absence of the respective mineral.

Sample	Porosity	Quartz	Calcite	Dolomite	Pyrite	K-feldspar	Plagioclase	Illite/smectite	Illite/mica	Kaolinite	Chlorite	Total clay	Kerogen
Core from Well A													
A1	5.76	40.70	26.47	0.92	2.50	0.33	1.17	6.91	4.33	0.00	0.00	11.24	10.92
A2	2.99	3.27	83.05	0.77	0.00	0.00	0.00	2.02	2.69	4.62	0.00	9.34	0.58
A3	7.96	36.03	22.29	3.42	3.82	0.81	1.79	6.91	6.26	0.00	0.00	13.18	10.7
A5	7.520	33.72	21.51	2.67	3.07	0.32	1.62	10.43	7.60	0.00	0.00	18.03	11.54
A7	4.73	5.06	1.31	57.33	4.22	0.00	1.03	8.53	3.28	12.83	0.00	24.64	1.68
A8	2.03	6.68	78.50	0.00	1.16	0.00	0.68	4.36	3.29	2.23	0.00	9.87	1.08
A2-1	4.96	4.91	76.28	0.00	0.69	0.00	0.00	1.98	1.72	0.52	0.00	4.22	8.94
A12	7.71	39.54	17.54	0.50	3.72	1.16	2.07	10.42	7.86	0.00	0.00	18.28	9.48
A3-1	6.42	37.79	19.15	2.69	5.88	0.25	1.93	9.83	6.47	0.00	0.00	16.29	9.60
A16	8.44	42.79	12.37	1.29	3.80	0.24	1.78	9.46	9.14	0.00	0.00	18.60	10.68
A18	8.50	46.05	12.88	0.32	3.54	0.56	2.17	7.33	7.65	0.00	0.00	14.97	11.00
A4-1	12.26	47.91	10.64	0.23	2.94	0.30	1.51	5.96	6.04	0.00	0.00	12.00	12.22
A18A	6.07	36.71	12.77	10.32	6.85	0.00	1.52	8.97	7.44	0.00	0.00	16.41	9.34
A18B	10.10	47.95	10.95	2.94	2.86	0.57	1.63	8.90	5.96	0.00	0.00	14.87	8.14
Core from Well G													
G2 ET	8.83	16.56	38.85	2.61	0.87	3.49	6.10	13.07	6.97	0.00	2.61	22.65	4.04
G3 ET	9.65	14.23	51.05	0.84	0.84	1.67	2.51	10.04	2.51	0.00	0.00	12.55	6.66
G4 ET	8.60	12.81	55.52	1.71	5.12	1.71	3.42	4.27	0.85	0.00	0.00	5.12	5.98
G5 ET	9.05	14.86	49.53	0.83	1.65	0.83	3.30	5.78	4.95	0.00	0.83	11.56	8.40
G6 ET	9.57	8.32	59.94	0.00	0.83	1.66	3.33	4.99	4.19	0.00	0.00	9.16	7.18
G7 ET	9.28	23.76	40.14	1.64	1.64	1.64	3.28	6.55	2.46	0.00	0.82	9.38	8.8
G8 ET	10.08	19.72	33.92	2.37	3.16	1.58	3.94	9.47	3.16	0.00	1.58	14.20	11.04
G9 ET	9.17	15.30	36.25	0.81	4.03	1.61	4.83	12.08	4.83	0.00	0.81	17.72	10.28
Core from Well N													
N1H1A	9.31	22.49	25.12	6.53	0.27	6.53	17.87	-	-	-	-	12.06	0.00
N1H11	30.26	12.83	41.15	1.53	0.35	1.95	5.30	-	-	-	-	6.63	0.00
N1H12	29.89	14.65	37.51	2.17	0.35	1.89	6.66	-	-	-	-	6.87	0.00
N1H17	23.35	18.78	26.21	1.38	0.77	3.53	11.88	-	-	-	-	14.10	0.00
N1H18	22.72	19.39	43.36	1.93	1.24	1.47	5.33	-	-	-	-	6.57	0.00
N1H20	24.21	20.69	23.95	1.67	0.45	3.79	12.58	-	-	-	-	12.66	0.00
N1H21	23.06	20.16	26.70	1.69	0.46	3.23	11.54	-	-	-	-	13.16	0.00
N1H22	25.38	21.12	23.13	2.16	0.45	3.36	13.73	-	-	-	-	10.67	0.00
N3H2	26.48	17.35	25.00	2.35	1.25	2.06	9.19	-	-	0.59	1.91	16.32	0.00
N3H4	25.30	13.15	6.87	5.53	2.32	4.48	12.62	-	-	1.49	3.21	29.73	0.00
N3H5	24.95	20.19	7.43	8.93	1.65	6.15	16.36	-	-	0.75	1.95	14.33	0.00
N3H7	31.02	17.59	9.10	9.66	1.38	4.41	14.76	-	-	0.89	2.14	12.07	0.00
N3H8	32.05	17.06	6.18	8.15	1.36	4.28	15.08	-	-	1.01	2.25	15.83	0.00
N3H10	24.12	24.05	6.75	5.92	1.52	6.68	18.67	-	-	0.76	1.89	12.29	0.00
N3H13	23.88	26.72	7.54	6.55	1.38	6.62	17.96	-	-	0.84	2.06	8.91	0.00
N3H15	3.97	26.89	25.83	4.90	2.11	6.72	20.55	-	-	0.77	2.11	9.03	0.00
N3H16	23.09	16.46	8.00	4.92	1.69	6.54	13.61	-	-	1.00	2.70	25.69	0.00
N3H25	11.90	24.40	19.47	4.93	1.94	6.34	14.17	-	-	0.88	2.82	16.30	0.00
N3H26	13.16	19.80	16.93	5.21	1.74	7.38	16.85	-	-	0.95	2.86	18.93	0.00
Core from Well Q													
Q4V	20.80	78.41	0.00	0.00	0.00	0.00	0.00	-	-	0.00	0.00	0.79	0.00
Q38V	16.30	79.52	0.00	0.00	0.00	0.00	0.00	-	-	0.00	0.00	4.19	0.00
Q49V	18.90	77.05	0.00	0.00	0.00	0.00	0.00	-	-	0.81	0.00	4.06	0.00

Table 4. Density ρ_b, SGR, K, U and Th measured from well logs corresponding to the 44 core samples.

Sample	$\rho\left(\frac{g}{cm^3}\right)$	SGR (API)	K (%)	U (ppm)	Th (ppm)
Core from Well A					
A1	2.38	77.41	0.91	5.87	3.99
A2	2.69	48.00	0.42	3.61	3.10
A3	2.45	61.17	0.64	4.58	3.58
A5	2.44	50.58	0.37	4.57	2.04
A7	2.76	97.74	0.49	10.21	2.05
A8	2.68	144.68	0.46	14.80	4.74
A2-1	2.48	130.68	0.85	12.17	4.92
A12	2.54	91.82	1.24	6.74	4.53
A3-1	2.47	65.79	1.03	4.98	2.37
A16	2.67	95.41	1.32	6.42	5.72
A18	2.43	69.35	0.85	5.02	3.92
A4-1	2.44	88.92	0.85	7.09	4.66
A18A	2.36	92.37	1.02	9.85	3.29
A18B	2.43	65.56	0.72	5.44	2.64
Core from Well G					
G2 ET	2.76	32.93	0.88	1.39	1.95
G3 ET	2.55	62.01	1.07	3.07	5.10
G4 ET	2.50	63.47	0.70	4.24	4.57
G5 ET	2.46	64.96	0.59	4.69	4.48
G6 ET	2.45	70.29	0.68	5.14	4.57
G7 ET	2.44	70.01	0.51	5.82	3.83
G8 ET	2.48	71.24	0.54	5.94	3.80
G9 ET	2.51	59.53	0.58	3.84	4.87
Core from Well N					
N1H1A	2.29	69.04	1.70	4.21	8.78
N1H11	2.26	48.94	1.35	2.70	6.78
N1H12	2.23	58.93	1.61	3.03	8.60
N1H17	2.25	53.33	1.49	2.69	7.88
N1H18	2.24	53.23	1.65	2.35	8.53
N1H20	2.24	56.41	1.49	2.73	8.59
N1H21	2.27	49.78	1.27	2.35	7.70
N1H22	2.26	60.70	1.34	2.71	9.70
N3H2	2.24	56.18	1.97	2.73	8.50
N3H4	2.23	42.18	1.60	2.68	5.12
N3H5	2.22	40.59	1.65	2.71	4.67
N3H7	2.35	34.09	1.57	2.10	4.27
N3H8	2.38	33.18	1.48	2.01	4.22
N3H10	2.36	31.11	1.58	1.41	4.89
N3H13	2.30	39.76	1.61	1.89	6.08
N3H15	2.29	38.64	2.01	2.13	5.33
N3H16	2.39	39.82	1.98	2.52	4.84
N3H25	2.26	44.65	1.78	2.92	5.25
N3H26	2.32	44.72	1.83	2.74	5.62
Core from Well Q					
Q4V	2.29	10.03	0.17	0.52	4.73
Q38V	2.42	52.76	1.08	3.27	8.84
Q49V	2.27	10.70	0.15	0.89	0.85

percentage of smectite in the illite/smectite ratio is between 10-20% for the core samples A2, A3, A16, A18, A18A, and A18B, 70-80% for A7, A8, and A12, and is not specified for A1, A2-1, A3-1, and A4-1. The ratio for illite/mica is not set for any of the core samples.

The lithology of the core samples from Well G corresponds to silty argillaceous limestone. The rock porosity measured is between 8.6 to 10.08%. The minerals that conform to the rock are quartz, calcite, dolomite, pyrite, K-feldspar, plagioclase, proportions of illite/smectite and illite/mica, and chlorite. The presence of kerogen is in the range of 4.04-11.04%. The percentage of smectite in the illite/smectite ratio is between 30-50%, but the percentage of mica in the illite/mica ratio is not specified for all core samples.

Set data from Well N comprises two subsets: 8 core samples for N1 and 11 for N3. The lithology of both subsets corresponds to fine-grained sandstone cemented by calcareous material, and there is the presence of clay minerals. The porosity measured is between 3.97 to 32.05%. The minerals present in N1 are quartz, calcite, dolomite, pyrite, K-feldspar, plagioclase, and clay minerals, where their type is not specified. N3 has the same minerals as N1, but for clay minerals, it is reported: proportions of illite/smectite and illite/mica where the respective concentration and ratio are not specified, kaolinite and chlorite.

The lithology for the core samples from Well Q comprised sandstone, shales, silty sandstone, claystone, and sandy claystone. The porosity measured is 20.8%, 16.30%, and 18.90% for Q4V, Q38V, and Q49V, respectively. The minerals reported are quartz, clay minerals, being its type not specified, and kaolinite.

3.2.2 Core-well comparison

The data used in the forward modeling of the 44 core samples have different scales, i.e., XRD is given in microns (μm), information from thin petrographic sections is in millimeters (mm), petrophysical analysis is performed on centimeter-scale samples, and Well logs are recorded on the centimeter scale. Therefore, to analyze if the sample is representative of the entire rock due to heterogeneity of the medium, we calculate the density ρ_{bc} considering the minerals and fluid concentration in the respective core samples and their respective densities (Table 1), and we compare it with their corresponding bulk densities ρ_b obtained from Well logs. We use density as a reference point because it is an intensive and isotropic property, and the intrinsic densities of each component are not scale-dependent.

Figure 6a shows a good fit for samples A1, A2, A3, and A3-1 for Well A. For Well G, the fit is good for G4 ET, G5 ET, G6 ET, and G7 ET samples (Figure 6b). Sub-set N1 of well N, N1H12, N1H20, N1H21, and N1H22 present a minor misfit (Figure 6c) but a poor correlation for the N3 set (Figure 6d). Samples Q4V and Q49V fit well for Well Q, but Q38V mismatch (Figure 6e). The misfit between ρ_b and ρ_bc is a relevant factor to consider as it will affect the modeling results.

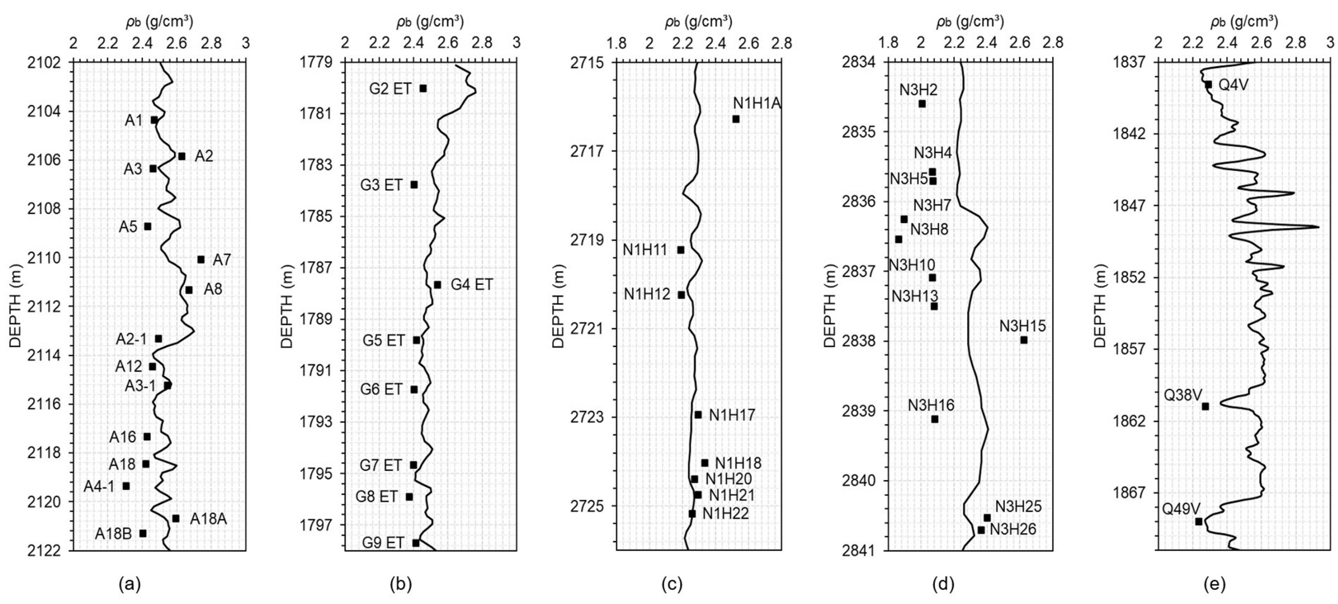

Figure 6. Misfit analysis between ρ_b from Well logs (black line) versus ρ_{bc} (squares) recalculated from core samples for the Wells: (a) A, (b) G, (c) Sub-set N1 of set N, (d) sub-set N3 of set N, and (e) Q. We consider that the misfits are associated to the variations of the sample scales and the heterogeneity of the medium.

3.2.3 Discussion

We choose for the radioactive minerals those fractional abundances of K, U, and Th that resulted in a very good fit between the simulated (K_s, U_s, Th_s, SGR_s) and the well log measured values of K_o, U_o, Th_o, and SGR_o given in Table 1.

The considered radioactive minerals from the core samples for Well A are calcite, dolomite, K-feldspar, plagioclase, mixtures of illite/smectite and illite/mica, kaolinite, and kerogen. Since the proportion of the illite/smectite mixture was unavailable for these samples, it was assumed to lie in 10% - 20% or 70% - 80%. We assigned a 50 to 50% ratio for the illite/mica mixture. For Well G, the radioactive minerals are calcite, dolomite, K-feldspar, plagioclase, illite/smectite, illite/mica, chlorite, and kerogen. Since the illite/smectite and illite/mica mixtures were not specified, we assigned 50 to 50% ratios. The radioactive considered minerals in the N1 core sample are calcite, dolomite, K-feldspar, plagioclase, and mica. For N3, the radioactive minerals considered are calcite, dolomite, K-feldspar, plagioclase, illite, smectite, kaolinite, and chlorite. The considered radioactive minerals for well Q are mica and kaolinite. We neglect quartz as a radioactive mineral in all the samples because it does not contribute significantly to the SGR modeled.

We analyze the results separately for K, U, Th, and SGR due to the scale differences of their units. We used the positive Pearson correlation coefficient (r) to measure the misfit between the simulated and observed data, where $r = 0$ means zero correlation, $0 < r <= 0.3$ represents a weak correlation, $0.3 < r <= 0.6$ is associated with a moderate correlation, $0.6 < r <= 0.9$ is a strong correlation, and $r > 0.9$ corresponds to a very high correlation (Akoglu, 2018; Taylor, 1990).

We used Equation 12 and the parameters listed in Table 5 for the respective radioactive minerals present in the five sample sets to simulate K (K_s). K observed (K_o) was established directly from the Well log (Figure 7). The relationship between K_s and K_o correlates with $r = 0.82$.

Equation 13 and the values indicated in Table 6 were used for the respective radioactive minerals present in the five sample sets to simulate U (U_s). U observed (U_o) was taken directly from the respective well logs (Figure 8). The correlation between U_s and U_o is $r = 0.83$.

We model Th (Th_s) with Equation 14 and the values indicated in Table 7 for the respective radioactive minerals in the five sample sets. Th observed (Th_o) is taken directly from the Well log (Figure 9). The misfit between Th_s and Th_o correlates with $r = 0.61$.

The correlation between SGR simulated modeled with Equation 10 (SGR_s) and SGR observed taken from the Well log (SGR_o) has a high correlation of $r = 0.57$ (Figure 10).

The forward modeling results show a strong correlation between simulated and observed data for K, U, and Th but a moderate correlation for SGR. The misfit is due not only to the difference between ρ_{bc} and ρ_c but also because we are assuming fixed concentrations and ratios for illite/smectite and illite/mica in set data A, B, and N3, and the clay is mica for N1 and Q.

Joint inversion with SGR, K, Th, and U was applied to improve the correlation by finding the concentrations of clay minerals that are not explicitly specified in the core information. The condition to be met is that the sum of the clay minerals must be equal to the total clay reported in each data set.

Joint inversion process minimizes the cost function relating to the observed and simulated data:

$$F_{min}=\|\mathbf{W}_d\,(\mathbf{d}(\mathbf{m})-\mathbf{d}_o\,)\|^2. \qquad (15)$$

Table 5. Fractional *K* (%) abundance for the respective radioactive minerals used in the five core sample sets. Void entries indicate the absence of the mineral.

Mineral	A	G	N1	N3	Q
Calcite	1.9	1.9	1.9	1.9	-
Dolomite	0	0	0	1.5	-
K-feldspar	7	7	7	7	-
Plagioclase	3	3	3	3	-
Mica	40	1	50	20	50
Illite	15	10	-	20	-
Smectite	6	6	-	7	-
Kaolinite	20	-	-	44	50
Chlorite	-	5	-	5	-
Kerogen	0	0	-	-	-

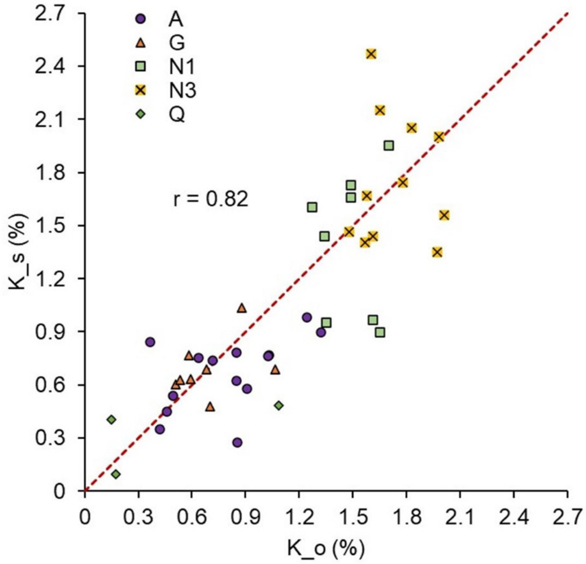

Figure 7. The general correlation between the K_s and K_o for the core samples: A (purple circles), G (red triangles), N1 (green squares), N3 (yellow squares), and Q (green diamonds). The Pearson correlation coefficient (r) is 0.82.

Table 6. Fractional *U* (ppm) abundance for the respective radioactive minerals used in the five core sample sets. Void entries indicate the absence of the mineral.

Mineral	A	G	N1	N3	Q
Calcite	10	2.5	3.5	6	-
Dolomite	10	10	8	10	-
K-feldspar	0.2	0.2	3	0.2	-
Plagioclase	0.02	0.02	5	0.02	-
Mica	5	5	5	4	40
Illite	5	1	-	3.5	-
Smectite	21	1	-	9	-
Kaolinite	1	-	-	1	1
Chlorite	-	0	-	0	-
Kerogen	66	62.5	-	-	-

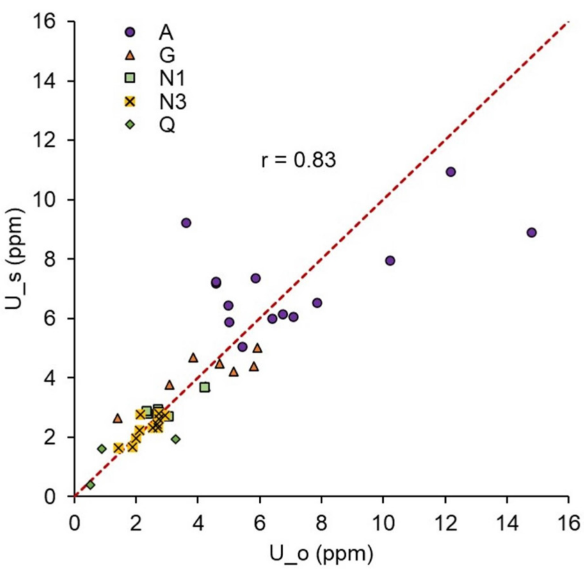

Figure 8. The general correlation between the U_s and U_o for the core sample sets: A (purple circles), G (red triangles), N1 (green squares), N3 (yellow squares), and Q (green diamonds). The Pearson correlation coefficient (r) is 0.83.

Table 7. Fractional abundance of *Th* (ppm) for the respective radioactive minerals used in the five core sample sets. Void entries indicate the absence of the mineral.

Mineral	A	G	N1	N3	Q
Calcite	1.9	1.9	1.9	1.9	-
Dolomite	0	0	0	1.5	-
K-feldspar	7	7	7	7	-
Plagioclase	3	3	3	3	-
Mica	40	1	50	20	50
Illite	15	10	-	20	-
Smectite	6	6	-	7	-
Kaolinite	20	-	-	44	50
Chlorite	-	5	-	5	-
Kerogen	0	0	-	-	-

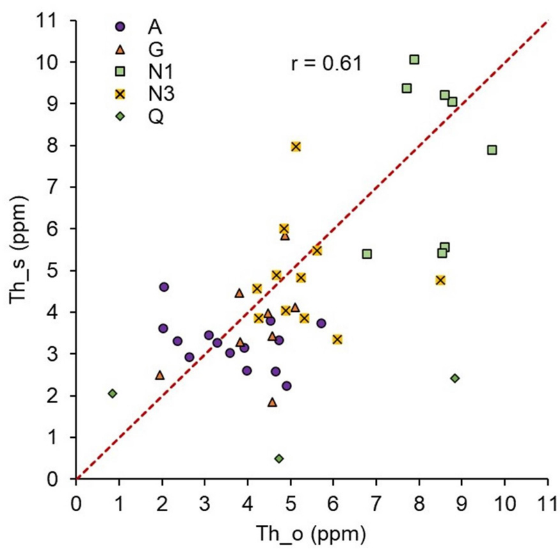

Figure 9. The general correlation between the Th_s and Th_o for the core sample sets: A (purple circles), G (red triangles), N1 (green squares), N3 (yellow squares), and Q (green diamonds). The Pearson correlation coefficient (r) is 0.61.

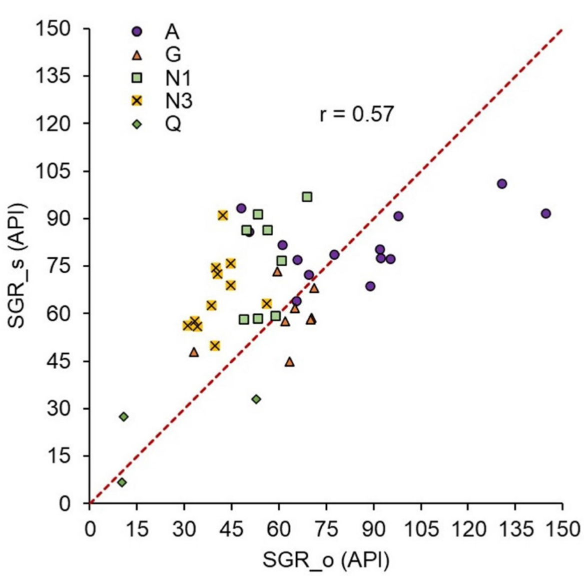

Figure 10. The general correlation between the SGR_s and SGR_o for the core sample sets: A (purple circles), G (red triangles), N1 (green squares), N3 (yellow squares), and Q (green diamonds). The Pearson correlation coefficient (r) is 0.57.

The vector $\mathbf{d}(\mathbf{m})$ contains the simulated data, and $\mathbf{d}_o$ the observed data:

$$\mathbf{d}(\mathbf{m})=[SGR\_s,K\_s,Th\_s,U\_s]^T, \tag{16}$$

$$\mathbf{d}_o=[SGR\_o,K\_o,Th\_o,U\_o]^T, \tag{17}$$

$\mathbf{W}_d$ represents the diagonal matrix of weight coefficient to account for different error scales and distribution of each input data and is calculated as the inverse of the standard deviation. The Nelder-Mead method was used to obtain the solution to the cost function optimization problem which gives a stable global minimum without the need to calculate functional derivatives (Nelder and Mead, 1965). The r improved to a strong correlation of 0.87, 0.85, 0.65, and 0.69 for K (Figure 11), U (Figure 12), Th (Figure 13), and SGR (Figure 14), respectively.

The correlation is further improved when joint inversion supports the forward modeling. Table 8 summarizes the correlation r for forward modeling with non-joint and joint inversion for the unknown mixture ratios.

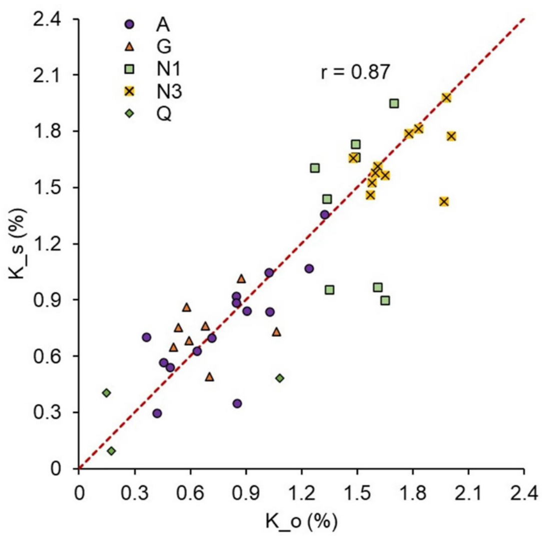

Figure 11. The correlation between the K_s and K_o improved after inverting for the unknown mixture ratios for core sample sets: A (purple circles), G (red triangles), N1 (green squares), N3 (yellow squares), and Q (green diamonds). The Pearson correlation coefficient (r) attained a value of 0.87.

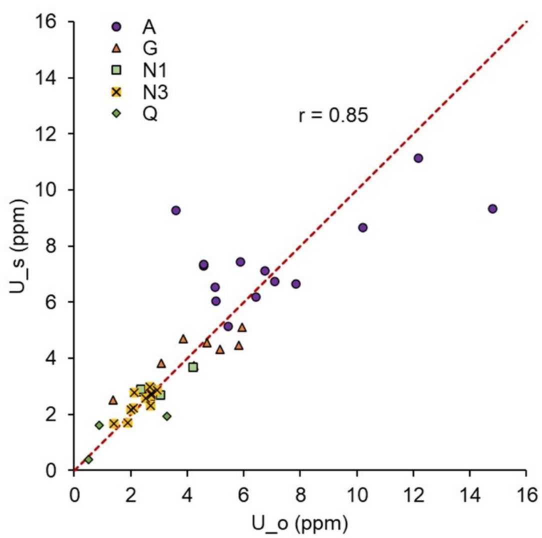

Figure 12. The correlation between the U_s and U_o improved after inverting for the unknown mixture ratios for core sample sets: A (purple circles), G (red triangles), N1 (green squares), N3 (yellow squares), and Q (green diamonds). The Pearson correlation coefficient (r) attained a value of 0.85.

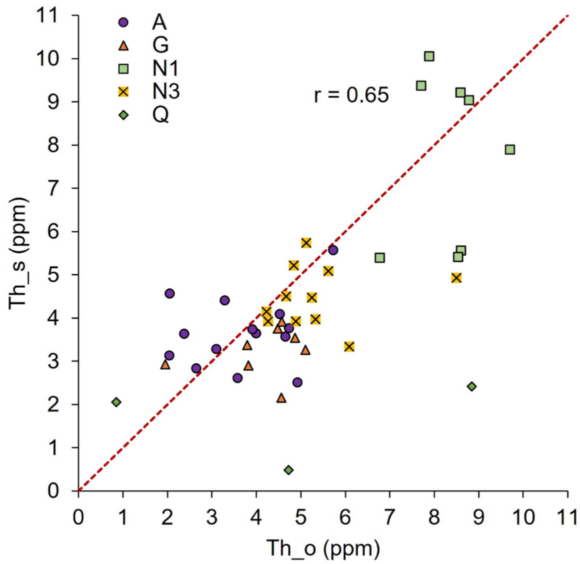

Figure 13. The correlation between the Th_s and Th_o improved after inverting for the unknown mixture ratios for core sample sets: A (purple circles), G (red triangles), N1 (green squares), N3 (yellow squares), and Q (green diamonds). The Pearson correlation coefficient (r) attained a value of 0.65.

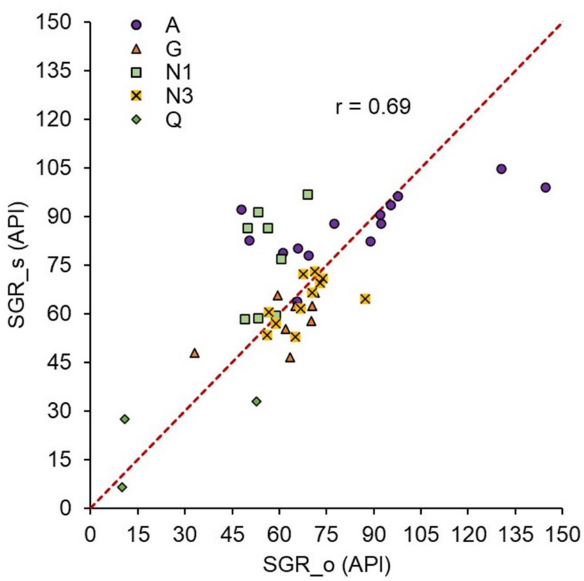

Figure 14. The correlation between the SGR_s and SGR_o improved after inverting for the unknown mixture ratios for core sample sets: A (purple circles), G (red triangles), N1 (green squares), N3 (yellow squares), and Q (green diamonds). The Pearson correlation coefficient (r) attained a value of 0.69.

Table 8. Pearson correlation coefficients (r) comparison between forward modeling with non-joint inversion and supported by the joint inversion.

	Non-joint inversion	Joint inversion
K (%)	0.82	0.87
U (ppm)	0.83	0.85
Th (ppm)	0.61	0.65
SGR (API)	0.57	0.69

4. Conclusions

We presented a new approach to improve SGR forward modeling by considering minerals with K^{40}, Th^{232}, and U^{238} content as radioactive sources that are uniformly distributed in the rock; furthermore, the measured radioactivity is proportional to the concentration of radioactive minerals, and the radioactivity is only attenuated by absorption of gamma-rays. The forward modeling approach foundation is based on radioactive attenuation theory.

The SGR forward modeling was tested in a synthetic rock of sandstone with clay minerals and brine-saturated pores to analyze the sensitivity to variations of illite/smectite and illite/mica mixtures over SGR. The results show that illite/smectite and illite/mica ratio variations impact the simulated K, U, Th, and SG. Thus, to determine the corresponding mixtures, it is recommended to include K, U, and Th in addition to SGR in the forward modeling. Moreover, the nonlinear trend between SGR versus clay concentration depends on the rock's bulk density.

Finally, we tested the proposed modeling for 44 core samples from four wells, where 22 correspond to shale gas and 22 to clastic formation. We evaluated the misfit using the Pearson correlation coefficient. For K, U, and Th, a strong correlation of 0.82, 0.83, and 0.61, respectively, is obtained, and a moderate correlation of 0.57 for SGR. However, the respective correlations improved to a strong correlation of 0.87, 0.85, 0.65, and 0.69 after joint inversion for the unknown illite/smectite and illite/mica mixtures. The strong correlation between the simulated and observed K, U, Th, and SGR support the viability of the proposed SGR forward modeling approach.

The proposed approach allows us to dispense with empirical equations and can improve petrophysical evaluations of oil reservoirs by quantifying the concentration of radioactive minerals, even distinguishing between clays and the presence of feldspars in hot sands, and the organic matter content can be calculated in formations with organic richness. Furthermore, it can be useful to identify the abundance of fractures in carbonate formations, since with the proposed approach a lower density with a higher radiative response can be modeled.

5. Acknowledgments

The author Francisco Miguel Lechuga Lagos expresses his gratitude to CONACYT for the scholarship granted to him and to the Postgraduate Program of Instituto Mexicano del Petróleo for the support provided. The authors thank Project 205862 of the SENER Hidrocarburos Sectoral Fund for allowing them to use information in developing this paper. NLOG.NL is also acknowledged for the information provided on its website. Special thanks to all the two anonymous reviewers and to Oscar C. Valdiviezo-Mijangos associated editor for their critical and constructive comments that helped to improve the manuscript quality, the anonymous reviewers and the associate editor for their important comments and technical corrections to improve this paper.

6. References

Akoglu, H. (2018). User's guide to correlation coefficients. *Turkish Journal of emergency medicine*, 18(3), 91–93. doi: 10.1016/j.tjem.2018.08.001

Adams, J. A. & Weaver, C. E. (1958). Thorium-to-uranium ratios as indicators of sedimentary processes: example of concept of geochemical facies. *AAPG Bulletin*, 42(2):387–430. doi: 10.1306/0BDA5A89-16BD-11D7-8645000102C1865D

Alharthy, N., Al Kobaisi, M., Torcuk, M. A., Kazemi, H., and Graves, R. (2012). *Physics and Modeling of Gas Flow in Shale Reservoirs*—paper presented at the Abu Dhabi International Petroleum Exhibition and Conference held in Abu Dhabi, UAE, 11-14 November 2012. doi: 10.2118/161893-MS

Bassiouni, Z. (1994). Gamma Ray Log. In Schenewerk, P. A. & Pert, D. M. (Eds.), *Theory, measurement, and interpretation of Well logs* (Vol. 4, pp. 146–158). Society of Petroleum Engineers.

Belknap, W. B., Dewan, J. T., Kirkpatrick, C., Mott, W. E., Pearson, A., and Rabson, W. (1959). Api calibration facility for nuclear logs, drilling and production practices API, reprinted in Gamma-Ray, Neutron and Density Logging: SPWLA Reprint volume (1978), Soc. Prof. Well Log Analysts, Houston, Texas (1959).

Bigelow, E. L. (2002). Determining Porosity, Formation Factor, and Shaliness. In Baker Atlas (Eds.) *Introduction to wireline log analysis* (pp. 137-184). Baker Hughes.

Bohacs, K. M. (1998). Contrasting expressions of depositional sequences in Mudrocks from Marine to non Marine Environs. In: Schieber, J., Zimmerle, W., Sethi, P. (Eds.), Shales and Mudstones (Vol. 1): Basin Studies, Sedimentology and PaleontologySchweizerbart'sche Verlagsbuchhandlung, Stuttgart, pp. 33-78

Bohacs, K. M. and Miskell-Gerhardt, K. (1998). Well-log expression of lake strata; controls of lake-basin type and provenance, contrasts with marine strata—paper presented at the AAPG Annual Meeting Expanded Abstracts, Tulsa, Oklahoma, p. A78.

Brannon, H. and Osoba, J. (1956). Spectral gamma-ray logging. Transactions of the AIME, 207(01): pp. 30-35.

Chudi, O. and Simon, R. (2012). Petrophysical characterization of radioactive sands-integrating well logs and core information: A case study in the Niger delta. Paper presented at the Nigeria Annual International Conference and Exhibition, Lagos, Nigeria, August 2012. doi: 10.2118/163020-MS

Clavier, C., Hoyle, W., and Meunier, D. (1971). Quantitative interpretation of thermal neutron decay time logs: part I fundamentals and techniques. *Journal of Petroleum Technology*, 23(06): 743-755. doi: 10.2118/2658-A-PA

Day-Stirrat, R. J., Hillier, S., Nikitin, A., Hofmann, R., Mahood, R., and Mertens, G. (2021). Natural gamma-ray spectroscopy (NGS) as a proxy for the distribution of clay minerals and bitumen in the cretaceous McMurray formation, Alberta, Canada. *FUEL*, 288. doi: 10.1016/j.fuel.2020.119513

Duderstadt, J. J. and Hamilton, L. J. (1976). Neutron Transport. In Wiley (Ed.), *Nuclear reactor analysis* (pp. 103–148). John Wiley & Sons.

Ehsan, M. S., Rahman, M. F., Tabassum, N., Prodhan, M. M. H., Pervin, S., Siraz, M. M., Rahman, A. M., Yeasmin, S., & Mahal, S. F. (2019). The activity concentration of radionuclides (226ra, 232nd, and 40k) in soil samples and associated health hazards in Natore, Kushtia, and Pabna districts of Bangladesh. *Journal of Bangladesh Academy of Sciences*, 43(2):169–180. doi: 10.3329/jbas.v43i2.45738

Ellis, D. V. and Singer, J. M. (2007). Gamma Ray Devices. In Springer (Ed.) *Well logging for earth scientists* (Vol. 692, pp. 267–288). Springer.

Evans, R. D. (1955). Attenuation and Absorption of Electromagnetic Radiation. In McGraw-Hill (Ed.) *The atomic nucleus* (pp. 711–745). McGraw-Hill New York.

Fertl, W. H. (1979). Gamma ray spectral data assists in complex formation evaluation. *Petrophysics*, 20(05).

Fertl, W. H., Chilingarian, G. V., & Yen, T. (1982). Use of natural gamma ray spectral logging in evaluation of clay minerals. *Energy Sources*, 6(4):335–360. doi: 10.1080/00908318208946036

Ge, X., Fan, Y., Cao, Y., Li, J., Cai, J., Liu, J., and Wei, S. (2016). Investigation of organic related pores in unconventional reservoir and its quantitative evaluation. *Energy & Fuels*, 30(6):4699–4709. doi: 10.1021/acs.energyfuels.6b00590

Gonzalez, J., Lewis, R., Hemingway, J., Grau, J., Rylander, E., & Schmitt, R. (2013). Determination of formation organic carbon content using a new neutron-induced gamma ray spectroscopy service that directly measures carbon—paper presented at the SPWLA 54th annual logging symposium.

Hertzog, R., Colson, L., Seeman, O., O'Brien, M., Scott, H., McKeon, D., Wraight, P., Grau, J., Ellis, D., Schweitzer, J., *et al.* (1989). Geochemical logging with spectrometry tools. *SPE Formation Evaluation*, 4(02):153–162. doi: 10.2118/16792-PA

Huang, R., Wang, Y., Cheng, S., Liu, S., and Cheng, L. (2015). Selection of logging-based TOC calculation methods for shale reservoirs: A case study of the Jiaoshiba shale gas field in the Sichuan basin. *Natural Gas Industry B*, 2(2-3):155–161. doi: 10.1016/j.ngib.2015.07.004

Huntley, D. J. & Baril, M. (1997). The K content of the K-feldspars being measured in optical dating or in thermoluminescence dating. *Ancient Tl,* 15(1):11–13.

Jacobi, D. J., Gladkikh, M., LeCompte, B., Hursan, G., Mendez, F., Longo, J., Ong, S., Bratovich, M., Patton, G. L., & Shoemaker, P. (2008). Integrated petrophysical evaluation of shale gas reservoirs—paper presented at the CIPC/SPE Gas Technology Symposium 2008 Joint Conference, Calgary, Alberta, Canada, June 2008. doi: 10.2118/114925-MS

Kethireddy, N., Chen, H., & Heidari, Z. (2014). Quantifying the effect of kerogen on resistivity measurements in organic-rich mudrocks. *Petrophysics*-The SPWLA Journal of Formation Evaluation and Reservoir Description, 55(02):136–146.

Killeen, P. (1982). Gamma-ray logging and interpretation. In Fitch A. A. (Ed.) *Developments in Geophysical Exploration Methods-3* (pp. 95–150). Springer.

Larionov, W. W. (1969). Method of natural radioactivity of rocks. In Nedra (Ed.) Borehole radiometry (pp. 74-129). Nedra, Moscow

Lewis, R., Ingraham, D., Pearcy, M., Williamson, J., Sawyer, W., & Frantz, J. (2004). New evaluation techniques for gas shale reservoirs—paper presented at the Reservoir symposium, Schlumberger, Houston, July 2004.

Lock, G. and Hoyer, W. (1971). Natural gamma-ray spectral logging. Paper presented at the SPWLA 12th Annual Logging Symposium, Dallas, Texas, May 1971.

Lüning, S. & Kolonic, S. (2003). Uranium spectral gamma-ray response as a proxy for organic richness in black shales: Applicability and limitations. *Journal of petroleum geology*, 26(2):153–174. doi: 10.1111/j.1747-5457.2003.tb00023.x

Mathis, G. L., Tittle, C., Rutledge, D., Mayer, R., & Ferguson, W. (1984). A spectral gamma ray (SGR) tool—paper presented at the SPWLA 25th Annual Logging Symposium, New Orleans, Louisiana, June 1984.

North, C. P. and Boering, M. (1999). Spectral gamma-ray logging for facies discrimination in mixed fluvial-eolian successions: A cautionary tale. *AAPG Bulletin*, 83(1):155–169. doi: 10.1306/00AA9A2A-1730-11D7-8645000102C1865D

Morys, M. (2020). *Spectral Gamma Ray Downhole Logging Tool* (U.S. Patent No. US 10,670,736 B2). Nabors Drilling Technologies USA, Inc., Houston, TX (US).

Morys, M. (2021). *Spectral Gamma Ray Downhole Logging Tool* (U.S. Patent No. US 11,119,226 B2). Nabors Drilling Technologies USA, Inc., Houston, TX (US).

Owen, J. D. (1966). A review of fundamental nuclear physics applied to gamma ray spectral logging. In *The Log Analyst*, 7(03).

Passey, Q., Creaney, S., Kulla, J., Moretti, F., & Stroud, J. (1990). A practical model for organic richness from porosity and resistivity logs. *AAPG Bulletin*, 74(12):1777–1794. doi: 10.1306/0C9B25C9-1710-11D7-8645000102C1865D

Passey, Q. R., Bohacs, K., Esch, W. L., Klimentidis, R., and Sinha, S. (2010). From oil-prone source rock to gas-producing shale reservoir–geologic and petrophysical characterization of unconventional shale-gas reservoirs—paper presented at the International Oil and Gas Conference and Exhibition in China, Beijing, China, June 2010. doi: 10.2118/131350-MS

Rhodes, D. & Mott, W. (1966). Quantitative interpretation of gamma-ray spectral logs. *Geophysics*, 31(2):410–418. doi: 10.1190/1.1439785

Russell, W. L. (1945). Relation of radioactivity, organic content, and sedimentation. *AAPG Bulletin*, 29(10):1470–1493. doi: 10.1306/3D933796-16B1-11D7-8645000102C1865D

Rutherford, E., & Soddy, F. (1902). LXIV. The cause and nature of radioactivity. —Part I. *The London, Edinburgh, and Dublin Philosophical Magazine and Journal of Science*, 4(23), 569–585. doi: doi.org/10.1080/14786440209462881

Schmoker, J. W. (1979). Determination of organic content of Appalachian Devonian shales from formation-density logs: Geologic notes. *AAPG Bulletin*, 63(9):1504–1509. doi: 10.1306/2F9185D1-16CE-11D7-8645000102C1865D

Schmoker, J. W. (1981). Determination of organic-matter content of Appalachian Devonian shales from gamma-ray logs. *AAPG Bulletin*, 65(7):1285–1298. doi: 10.1306/03B5949A-16D1-11D7-8645000102C1865D

Schnyder, J., Ruffell, A., Deconinck, J.-F., and Baudin, F. (2006). Conjunctive use of spectral gamma-ray logs and clay mineralogy in defining late Jurassic–early Cretaceous palaeoclimate change (Dorset, UK). *Paleogeography, Palaeoclimatology, Palaeoecology*, 229(4):303–320. doi: 10.1016/j.palaeo.2005.06.027

Schön, J. H. (2015). Nuclear/Radioactive Properties. In Elsevier (Ed.) *Physical properties of rocks: Fundamentals and principles of petrophysics* (pp. 119 – 166). Elsevier.

Sen, S. K. (1959). Potassium content of natural plagioclases and the origin of antiperthites. The Journal of Geology, 67(5):479–495. doi: 10.1086/626602

Serra, O. (1984). Natural gamma-ray spectrometry. In Elsevier (Ed.) *Fundamentals of well-log interpretation, the acquisition of logging data* (pp. 113 – 133). Elsevier Science Pub. Co., Inc., New York, NY.

Serra, O., Baldwin, J., & Quirein, J. (1980). Theory, interpretation, and practical applications of natural gamma ray spectroscopy—paper presented at the SPWLA 21st Annual Logging Symposium, Lafayette, Louisiana, July 1980.

Steiner, S., Ahsan, S. A., Raina, I., Dasgupta, S., & Lis, G. P. (2016). Interpreting total organic carbon TOC in source rock oil plays—paper presented at the Abu Dhabi International Petroleum Exhibition & Conference, Abu Dhabi, UAE, November 2016. doi: 10.2118/183050-MS

Stieber, S. (1970). Pulsed neutron capture log evaluation-Louisiana Gulf coast—paper presented at the Fall Meeting of the Society of Petroleum Engineers of AIME, Houston, Texas, October 1970. doi: 10.2118/2961-MS

Swanson, V. E. (1960). Oil yield and uranium content of black shales. Technical report, Geological Survey, Washington, DC (USA).

Taylor, R. (1990). Interpretation of the correlation coefficient: a basic review. *Journal of diagnostic medical sonography*, 6(1), 35–39.

Tittman, J. (1966). Radiation logging: Physical Principles. Petroleum Engineering Conference. University of Kansas. In Lawson B. L. & Hoyer G. R. (Eds.) *Gamma Ray, Neutron and Density Logging* L. I. SPWLA

Van der Boor, M. (2014). Modelling the spectral gamma-ray log: The influence of provenance and selective transport: Master's thesis, Delft University of Technology.

Wang, J., Gu, D., Guo, W., Zhang, H., & Yang, D. (2019). Determination of total organic carbon content in shale formations with regression analysis. Journal of Energy Resources Technology, 141(1). doi: 10.1115/1.4040755

Wang, P., Chen, Z., Pang, X., Hu, K., Sun, M., and Chen, X. (2016). Revised models for determining TOC in shale play: Example from Devonian Duvernay shale, western Canada sedimentary basin. Marine and Petroleum Geology, 70:304–319. doi: 10.1016/j.marpetgeo.2015.11.023

Yuguchi, T., Yagi, K., Sasao, E., and Nishiyama, T. (2021). K-ar geochronology for hydrothermal k-feldspar within plagioclase in a granitic pluton: Constraints on timing and thermal condition for hydrothermal alteration. Heliyon, 7(4): e06750. doi: 10.1016/j.heliyon.2021.e06750